Extreme Hardening of Pb at High Pressure and Strain Rate

A. Krygier, P. D. Powell, J. M. McNaney, C. M. Huntington, S. T. Prisbrey, B. A. Remington, R. E. Rudd, D. C. Swift, C. E. Wehrenberg, A. Arsenlis, H.-S. Park, P. Graham, E. Gumbrell, M. P. Hill, A. J. Comley, and S. D. Rothman

Phys. Rev. Lett. **123**, 205701 — Published 11 November 2019

DOI: 10.1103/PhysRevLett.123.205701

Extreme hardening of Pb at high pressure and strain-rate

A. Krygier,* P. D. Powell, J. M. McNaney, C. M. Huntington, S. T. Prisbrey, B. A. Remington, R. E. Rudd, D. C. Swift, C. E. Wehrenberg, A. Arsenlis, and H.-S. Park
Lawrence Livermore National Laboratory, 7000 East Ave, Livermore, CA 94550 USA

P. Graham, E. Gumbrell, M. P. Hill, A. J. Comley, and S. D. Rothman
Atomic Weapons Establishment, Aldermaston, Reading, Berkshire, RG7 4PR, United Kingdom
(Dated: October 15, 2019)

We study the high-pressure strength of Pb and PbSb at the National Ignition Facility. We measure Rayleigh-Taylor growth of pre-formed ripples ramp compressed to ∼400 GPa peak pressure, among the highest-pressure strength measurements ever reported on any platform. We find agreement with 2D simulations using the Improved Steinberg-Guinan strength model for body-centered-cubic Pb; the PbSb alloy behaves similarly within the error bars. The combination of high-rate, pressure-induced hardening and polymorphism yield an average inferred flow stress of ∼3.8 GPa at high pressure, a ∼250-fold increase, changing Pb from soft to extremely strong.

Material deformation at high pressure and strain rate is a burgeoning research topic with applications in geophysics, inertial fusion, and ballistic penetration and advanced armor design [1, 2]. While direct dynamic strength, or flow stress, measurements under high-strain-rate, high-pressure conditions exceeds current capabilities, there are several techniques from which it can be inferred, including ramp-release [3], X-ray diffraction [4–6], and EXAFS [7]. We compare *in situ* plastic flow measurements to predictions from hydrodynamics simulations that include flow stress models. Our method, which builds upon the concept pioneered by Barnes et al. [8] and the development of hohlraum-based, reservoir-gap ramp drives [9], accelerates a sample with preformed sinusoidal ripples, while maintaining high-pressure conditions within the sample (see Fig. 1). As the sample is accelerated, the ripples grow via Rayleigh-Taylor (RT) instability [10, 11] and are radiographically characterized [12, 13]. The working principle of these measurements is that RT growth of the ripples is suppressed by the material's flow stress: the greater the flow stress, the less the ripple growth, for the same acceleration and Atwood number.

The crystallographic structure of a material is a key factor influencing its strength, since the lattice structure affects the Peierls stress (the barrier to dislocation movement through the crystal lattice). For example, body-centered-cubic (bcc) metals like Ta and V have a relatively large strength even at low strain due to high Peierls stress. On the contrary, face-centered-cubic (fcc) metals like Pb often have comparatively lower ambient strength and different hardening behavior, since dislocations glide more easily with a lower Peierls barrier. Much work using the RT growth technique has focused on Ta and V [12, 13], which were expected to stay in the bcc phase throughout the experiments; our team is also currently investigating shock-melted Cu. While ambient Pb forms the fcc phase, the expected phase transformation to bcc at ∼50 GPa [14–17] should significantly change the flow stress behavior in our experiment (see Fig. 2). However, no flow stress data for Pb currently exist at these high pressures to test this hypothesis and the predictions of the Pb flow stress models.

Lead is commonly alloyed with antimony to increase strength for applications ranging from lead-acid batteries (∼4-10wt%) [23, 24] to bullets (∼2-5wt%) [25]. In antimonial lead with more Sb than the 3.5wt% solubility limit and less than the 11.2wt% eutectic concentration, the grains are predominantly Pb with a small amount of fine-scale Sb rod-like particles with Pb-Sb eutectic at the grain boundaries [24]. Alloying with 4wt% Sb results in 4× increase in strength at ambient conditions and the relatively low strain rate of $10^3 s^{-1}$ (47 MPa vs. 12 MPa at strain (ε) = 0.15) [26, 27]. It is an open question whether this kind of alloying increases high-pressure dynamic strength. This motivates a new capability to increase sample size allowing side-by-side measurements of pure and alloyed metals subjected to identical drives.

In this Letter, we present results of experiments used to infer the flow stress in Pb and Pb-4wt%Sb at peak pressures of ∼400 GPa and strain rate ∼ 10^6-10^8 s^{-1}, determined by simulations. We use a novel, foam-based multi-layer expanding plasma drive [9, 12, 28]] that prevents melting at these pressures despite lead's low ambient melting temperature and shock Hugoniot melting pressure (∼54 GPa) [15, 29]. A time series of five X-ray radiographs characterize the growth of pre-formed ripples in experiments at the National Ignition Facility (NIF), similar to experiments using the Omega laser facility at lower peak pressures (∼100 GPa) [13, 30, 31]. We evaluate different flow stress models by their ability to reproduce these measurements in radiation hydrodynamic simulations.

The original Steinberg-Guinan (SG) model [32] and the newer Improved Steinberg-Guinan (ISG) model [20] are the only available dynamic flow stress models for Pb. Both models assume that the pressure and temperature dependence of the flow stress follows the shear modu-

lus. However, the SG model parameters are extrapolated to high pressure from measurements of ambient fcc Pb. Rudd et al. [20] addressed this issue with the ISG model, which is based on the high-pressure bcc phase and predicts 65% larger flow stress than the SG model in our experimental conditions. Lacking experimental data in this regime, the shear modulus for the ISG model was calculated using density functional theory (DFT) and quantum molecular dynamics (QMD), which explicitly account for crystalline structure. The ISG model is intended for high-pressure, high-rate deformation, but is not explicitly rate dependent [33–35] or designed to describe slip-to-twinning transitions [36].

Figure 1 shows our experimental setup. We use a reservoir-gap plasma drive generated by heating a hohlraum with 160 NIF beams (∼800 kJ); the reservoir is a multi-layer density gradient stack [37] (see supplementary materials) that expands across a gap, ramp compressing the sample as it stagnates. This technique shapes the drive and prevents melting in the rippled sample. The ripple amplitudes and substrate thickness are chosen to produce sufficient radiographic contrast while preventing degradation from effects like feedthrough [38] and non-linear ripple growth. Feedthrough occurs when the sample is hydrodynamically thin and the ripple growth produces sufficient flow to form unwanted ripples on the rear surface. We find no evidence of non-linear growth in the ripple lineouts and mitigate feedthrough with the design. Characterization of the Pb and Pb-4wt%Sb samples were performed via scanning electron microscope (SEM) and energy dispersive X-ray analysis (EDAX). We find that the grain sizes are ∼10s μm for Pb and ∼5 μm for Pb-4wt%Sb; in the alloy, Sb atoms mostly reside along the Pb grain boundaries.

The driven samples are radiographed face-on using a high-energy (>25 keV) X-ray source generated from an Ag foil heated with 12 tightly focused NIF beams. High-resolution 1D imaging is produced using a wedged slit (15 μm × 300 μm, ∼ 7° opening angle). The image plate data are digitized into photo-stimulated luminescence (PSL), which is linearly related to X-ray dose. We use an Au knife edge to derive the modulation transfer function (MTF) [39] and correct for source size effects [40, 41]. The corrected amplitude η is calculated from the observed amplitude in PSL, η_{observed}, using Eq. (1).

$$\eta = \frac{\eta_{\text{observed}}}{\text{MTF}(\lambda)}[PSL] \tag{1}$$

The *in situ* areal density ripple amplitude $(\rho\,\Delta\text{R})_{driven}$ is determined from η using a step-calibration table constructed with Pb/Pb-4wt%Sb steps. We characterize the ripple growth by the growth factor GF:

$$\text{GF} = \frac{(\rho\,\Delta\text{R})_{driven}}{(\rho\,\Delta\text{R})_{initial}}. \tag{2}$$

The thermodynamic history is determined by combined experiment and simulation. The plasma drive loading is characterized by matching the surface motion of a witness sample recorded by VISAR on a separate shot (N150608-04) with LASNEX radiation hydrodynamics simulations [42] as described by Prisbrey et al. [42]. This drive is applied to the rippled sample package in a hydrodynamics simulation using the ARES code [43]. Temporal histograms of the Pb pressure and ISG flow stress are shown in Fig. 4 (a) and (b), respectively; also shown in (a), the calculated ripple growth factor, ripple growth rate, and tracer particles.

The sample is initially shocked into the hexagonal-close-packed (hcp) phase region before compression into the bcc phase region, the observed phase in our conditions [17]. After a series of reverberations driving the Pb to ∼100-200 GPa, the sample reaches peak pressure of ∼400 GPa at ∼50 ns, corresponding to peak ISG flow stress of ∼4.5 GPa. The average pressure throughout the sample is held at ∼350 GPa for ∼7 ns and then releases to 200-250 GPa. The other thermodynamic variables largely follow qualitatively similar paths, though the rear of the sample is heated an extra ∼500-1000 K by a shock wave that appears briefly due to coalescence of multiple waves around 45 ns. This is not expected to significantly affect our growth factor measurements as the difference is only ∼5-10% of the calculated melting temperature and both are below melt.

Figure 5 shows experimental growth factor data vs. probe delay. The upper-left inset shows full growth curves with an extra curve using ISG but using the density of Pb-4wt%Sb. The bottom inset shows the driven experimental ripple growth for Pb samples at 55 ns and 65 ns probe time, showing no evidence of non-linear growth consistent with the design. All data are taken when the model predictions start differentiating at peak pressure (55 ns) and later during release. While most of the distinguishing growth occurs during the highest-pressure conditions, the integrated nature of our platform enables meaningful measurements when the sample is releasing from the highest-pressure state. As expected, the no-strength simulations predict the largest growth and are beyond the experimental error bars when they are sufficiently separated from the other models. The fcc-based SG model predictions improve on the no-strength case and overlap the error bars in a few cases, but clearly and systematically over-predict the ripple growth. Finally, the stronger, bcc-based ISG model reproduces the data well, with the error bars overlapping the model prediction at each datum.

Despite the polymorphism exhibited by lead across the range of experimental conditions, we only consider single-phase flow stress models. This is possible because the ripple growth predominantly occurs while Pb is in the bcc phase at peak acceleration and pressure. Furthermore, the growth factor is small (<1.5 in all models) and

growth factor curves for the different flow stress models do not differentiate until well after the sample crosses the hcp-bcc phase boundary at $\sim$ 40 ns. Additionally, the ripple growth rate and pressure histogram shown in Fig. 4 (a) are highly resemblant indicating that the largest growth rates occur while the sample is at the highest pressures. This is consistent with standard RT growth since the largest acceleration occurs for the largest jumps in pressure.

The flow stress calculated by the ISG model, which reproduces our experimental growth factor data, is shown in Fig. 4(b). The inferred flow stress averaged across the high-pressure plateau spanning $\sim$49-56 ns is $\sim$3.8 GPa, representing a $\sim$250$\times$ increase over ambient. While this value is high, it is comparable to the 6 GPa inferred flow stress for Ta at 100 GPa [13] and 2.5 GPa inferred flow stress found at 90 GPa peak pressure in V [12]. While these flow stresses are all of the same order of magnitude, the inferred Pb hardening is much higher than the $\sim$8$\times$ for Ta inferred using the Livermore Multiscale Strength (LMS) model, which found very high dislocation density, approaching saturation [34], where the corresponding Taylor hardening dwarfs other microstructural contributions [13]. While ISG does not include the same detailed physics as LMS, we expect any well-behaved flow stress model that could reproduce our experimental data to yield similar values for the average flow stress during ripple growth, independent of the mechanism.

Beyond the hardening mechanisms Pb shares with Ta, we need to consider whether the flow stress of Pb in the RT experiments is affected by phase transformation, specifically in two possible ways: (a) the flow stress in the high-pressure bcc phase of Pb may be greater due to microstructural differences resulting from the phase transformation, and (b) the flow stress increase may be greater due to lower strength of the initial (fcc) metal. First consider case (a), such as in iron. Iron RT-experiments have been performed with peak pressure of $\sim$100 GPa, whose data were consistent with flow stress >40 GPa [31]. Separate EXAFS measurements made at peak pressure 560 GPa were consistent with an upper limit of $\sim$70 GPa attributed to significant plastic work heating [7]. It has been suggested that the high flow stress of iron is caused by Taylor hardening due to dislocations associated with the $\alpha-\epsilon$ phase transformation, a reduction in dislocation mobility in the hcp phase, or grain-size strengthening (the Hall-Petch effect) related to an ultra-fine grain structure. For example, formation of 2-15 nm sized grains has been reported when single crystal iron is shocked across the $\alpha-\epsilon$ phase boundary [44]. While Pb crosses the hcp and bcc phase boundaries in the RT experiment, its flow stress may be significantly lower than irons since it is deforming in a cubic phase rather than a low-symmetry phase and unlike iron it does not undergo strong volume collapse at either transition. Furthermore, recent diffraction experiments see no evidence of formation of <10 nm grains under dynamic compression in this regime [17].

The growth factor data in Fig. 5 show no difference between Pb and Pb-4wt%Sb beyond the experimental error bars (described in supplementary materials). This implies similar flow stress behavior (i.e., no significant alloy strengthening) as the alloy is only 1.6% less dense than the Pb and therefore experiences very similar hydrodynamic conditions. While there are small differences between the respective equations of state [45], our experiments are designed to minimize these effects. This absence of alloy hardening is in contrast to the ambient behavior where alloying with 4wt% Sb produces 4$\times$ hardening [26, 27]. The unalloyed Pb shows similarly high flow stress. The agreement in the Pb and Pb-4wt%Sb growth factor data therefore suggests that the Taylor hardening together with pressure hardening (and possibly twinning) dwarfs any alloy-related hardening including alloy-induced grain boundary segregation hardening arising from the Sb, which is mostly distributed on the grain boundaries, and other microstructural changes.

The technique described here can be used to probe the flow stress of multiple samples simultaneously at pressures up to $\sim$400 GPa. The high energy drive at the NIF enables a large hohlraum and thus a large planar drive combined with a low-density foam-based multilayer reservoir to keep the temperature below melt during compression. The observed growth factor for Pb is described well by simulations using the ISG flow stress model for high-pressure bcc Pb, without explicitly accounting for the transformations to reach bcc or changes to the grain structure or any plastic reversion during release [46]. The inferred peak flow stress of $\sim$4.5 GPa and plateau average of $\sim$3.8 GPa is much higher than at ambient conditions. The Pb-4wt%Sb alloying has no measurable effect on the flow stress. Whether these properties are common to other metals and alloys remains an interesting, open question suitable for this platform. These are among the highest-pressure flow stress data ever recorded on any platform and the first to investigate the role of alloy strengthening in this regime.

This work was performed under the auspices of the U.S. Department of Energy by Lawrence Livermore National Laboratory under Contract DE-AC52-07NA27344.

* krygier1@llnl.gov

[1] R. E. Rudd, T. C. Germann, B. A. Remington, and J. S. Wark, MRS Bulletin **35**, 999 (2010).
[2] B. A. Remington, R. E. Rudd, and J. S. Wark, Physics of Plasmas **22**, 090501 (2015).
[3] J. L. Brown, C. S. Alexander, J. R. Asay, T. J. Vogler, and J. L. Ding, Journal of Applied Physics **114**, 223518 (2013).
[4] A. K. Singh, C. Balasingh, H.-K. Mao, R. J. Hemley, and J. Shu, Journal of Applied Physics **83**, 7567 (1998).

[5] S. Merkel, J. Phys.: Condens. Matter **18**, S949 (2006).

[6] A. J. Comley, B. R. Maddox, R. E. Rudd, S. T. Prisbrey, J. A. Hawreliak, D. A. Orlikowski, S. C. Peterson, J. H. Satcher, A. J. Elsholz, H.-S. Park, B. A. Remington, N. Bazin, J. M. Foster, P. Graham, N. Park, P. A. Rosen, S. R. Rothman, A. Higginbotham, M. Suggit, and J. S. Wark, Physical Review Letters **110**, 115501 (2013).

[7] Y. Ping, F. Coppari, D. G. Hicks, B. Yaakobi, D. E. Fratanduono, S. Hamel, J. H. Eggert, J. R. Rygg, R. F. Smith, D. C. Swift, D. G. Braun, T. R. Boehly, and G. W. Collins, Phys. Rev. Lett. **111**, 065501 (2013).

[8] J. F. Barnes, P. J. Blewett, R. G. McQueen, K. A. Meyer, and D. Venable, Journal of Applied Physics **45**, 727 (1974).

[9] J. Edwards, K. T. Lorenz, B. A. Remington, S. Pollaine, J. Colvin, D. Braun, B. F. Lasinski, D. Reisman, J. M. McNaney, J. A. Greenough, R. Wallace, H. Louis, and D. Kalantar, Phys. Rev. Lett. **92**, 075002 (2004).

[10] Y. Zhou, Physics Reports **720-722**, 1 (2017).

[11] Y. Zhou, Physics Reports **723-725**, 1 (2017).

[12] H.-S. Park, K. T. Lorenz, R. M. Cavallo, S. M. Pollaine, S. T. Prisbrey, R. E. Rudd, R. C. Becker, J. V. Bernier, and B. A. Remington, Physical Review Letters **104**, 135504 (2010).

[13] H.-S. Park, R. E. Rudd, R. M. Cavallo, N. R. Barton, A. Arsenlis, J. L. Belof, K. J. M. Blobaum, B. S. Eldasher, J. N. Florando, C. M. Huntington, B. R. Maddox, M. J. May, C. Plechaty, S. T. Prisbrey, B. A. Remington, R. J. Wallace, C. E. Wehrenberg, M. J. Wilson, A. J. Comley, E. Giraldez, A. Nikroo, M. Farrell, G. Randall, and G. T. Gray, Phys. Rev. Lett. **114**, 065502 (2015).

[14] C. A. Vanderborgh, Y. K. Vohra, H. Xia, and A. L. Ruoff, Phys. Rev. B **41**, 7338 (1990).

[15] A. Dewaele, M. Mezouar, N. Guignot, and P. Loubeyre, Physical Review B **76**, 144106 (2007).

[16] P. Song and L. Cai, Physica B: Physics of Condensed Matter **405**, 1509 (2010).

[17] A. Lazicki, private communication (2019).

[18] A. Kuznetsov, V. Dmitriev, L. Dubrovinsky, V. Prakapenka, and H. Weber, Solid State Communications **122**, 125 (2002).

[19] H. K. Mao, Y. Wu, J. F. Shu, J. Z. Hu, R. J. Hemley, and D. E. Cox, Solid State Communications **74**, 1027 (1990).

[20] R. E. Rudd, L. H. Yang, P. D. Powell, P. Graham, A. Arsenlis, R. M. Cavallo, A. G. Krygier, J. M. McNaney, S. T. Prisbrey, B. A. Remington, D. C. Swift, C. E. Wehrenberg, and H.-S. Park, AIP Conference Proceedings **1979**, 070027 (2018).

[21] C. Dai, H. Tan, and H. Geng, Journal of Applied Physics **92**, 5019 (2002).

[22] S. Marsh, *LASL Shock Hugoniot Data* (University of California Press, 1980).

[23] R. S. Dean, W. E. Hudson, and M. F. Fogler, Industrial and Engineering Chemistry **17**, 1246 (1925).

[24] J. Perkins, Materials Science and Engineering **28**, 167 (1977).

[25] C. A. Johnson, H. Moench, P. Wersin, P. Kugler, and C. Wenger, Journal of Environmental Quality **34**, 248 (2005).

[26] S. El-Gamal, G. Mohammed, and E. E. Abdel-Hady, Amer. J. Mater. Sci. **5**, 97 (2015).

[27] V. A. M. Cristino, P. A. R. Rosa, and P. A. F. Martins, Tribology Transactions **55**, 652 (2012).

[28] S. T. Prisbrey, H.-S. Park, B. A. Remington, R. Cavallo, M. May, S. M. Pollaine, R. Rudd, B. Maddox, A. Comley, L. Fried, K. Blobaum, R. Wallace, M. Wilson, D. Swift, J. Satcher, D. Kalantar, T. Perry, E. Giraldez, M. Farrell, and A. Nikroo, Physics of Plasmas **19**, 056311 (2012).

[29] B. K. Godwal, C. Meade, R. Jeanloz, A. Garcia, A. M. Y. Y. Liu, and M. L. Cohen, Science **248**, 462 (1990).

[30] H.-S. Park, B. A. Remington, R. C. Becker, J. V. Bernier, R. M. Cavallo, K. T. Lorenz, S. M. Pollaine, S. T. Prisbrey, R. E. Rudd, and N. R. Barton, Physics of Plasmas **17**, 056314 (2010).

[31] C. M. Huntington, J. L. Belof, K. J. M. Blobaum, R. M. Cavallo, N. B. Kostinsko, B. R. Maddox, H. S. Park, C. Plechaty, R. Rudd, D. W. Swift, R. J. Wallace, S. V. Weber, C. Wehrenberg, M. J. Wilson, and B. A. Remington, AIP Conf. Proc. **1793**, 110007 (2017).

[32] D. J. Steinberg, S. G. Cochran, and M. W. Guinan, J. Appl. Phys. **51**, 1498 (1980).

[33] N. R. Barton, J. V. Bernier, R. Becker, A. Arsenlis, R. Cavallo, J. Marian, M. Rhee, H.-S. Park, B. A. Remington, and R. T. Olson, Journal of Applied Physics **109**, 073501 (2011).

[34] N. R. Barton and M. Rhee, Journal of Applied Physics **114**, 123507 (2013).

[35] D. L. Preston, D. L. Tonks, and D. C. Wallace, Journal of Applied Physics **93**, 211 (2003).

[36] C. E. Wehrenberg, D. McGonegle, C. Bolme, A. Higginbotham, A. Lazicki, H. J. Lee, B. Nagler, H.-S. Park, B. A. Remington, R. E. Rudd, M. Sliwa, M. Suggit, D. Swift, F. Tavella, L. Zepeda-Ruiz, and J. S. Wark, Nature **550**, 496 (2017).

[37] Y. P. Opachich, J. A. Koch, M. J. Haugh, E. Romano, J. J. Lee, E. Huffman, F. A. Weber, J. W. Bowers, L. R. Benedetti, M. Wilson, S. T. Prisbrey, C. E. Wehrenberg, T. F. Baumann, J. M. Lenhardt, A. Cook, A. Arsenlis, H.-S. Park, and B. A. Remington, Review of Scientific Instruments **87**, 073706 (2016).

[38] S. T. Weir, E. A. Chandler, and B. T. Goodwin, Phys. Rev. Lett. **80**, 3763 (1998).

[39] H. H. Barrett and W. Swindell, *Radiological Imaging: The Theory of Image Formation, Detection, and Processing* (Academic Press, 1981).

[40] U. Neitzel, E. Buhr, G. Hilgers, and P. R. Granfors, Medical Physics **31**, 3485 (2004).

[41] E. Gumbrell, J. M. McNaney, C. M. Huntington, A. G. Krygier, and H.-S. Park, Review of Scientific Instruments **89**, 10G118 (2018).

[42] G. B. Zimmerman and W. L. Kruer, Comments in Plasma Physics and Controlled Fusion **2**, 51 (1975).

[43] R. M. Darlington, T. L. Mcabee, and G. Rodrigue, Computer Physics Communications **135**, 58 (2001).

[44] J. A. Hawreliak, D. H. Kalantar, J. S. Stölken, B. A. Remington, H. E. Lorenzana, and J. S. Wark, Physical Review B **78**, 220101 (2008).

[45] S. D. Rothman, J.-P. Davis, J. Maw, C. M. Robinson, K. Parker, and J. Palmer, . Phys. D: Appl. Phys. **38**, 733 (2005).

[46] M. Sliwa, D. McGonegle, C. Wehrenberg, C. A. Bolme, P. G. Heighway, A. Higginbotham, A. Lazicki, H. J. Lee, B. Nagler, H. S. Park, R. E. Rudd, M. J. Suggit, D. Swift, F. Tavella, L. Zepeda-Ruiz, B. A. Remington, and J. S. Wark, Phys. Rev. Lett. **120**, 265502 (2018).

FIGURES

Figure 1. Cutaway diagram of the experimental setup including the hohlraum, multi-layer ablator/reservoir, rippled sample package, and backlighter. Bottom-left, initial ripples and ripple-growth simulations with and without strength.

Figure 2. Pressure-temperature conditions traversed in the RT experiment up to 80 ns, as simulated, plotted on the Pb phase diagram. The solid boundaries and melting curve up to 80 GPa are from Dewaele et al. [15] including the fcc-hcp phase boundary from Kuznetsov et al. [18] and the zero-temperature hcp-bcc transition from Mao et al. [19]. Above 80 GPa, the melting curve is based on the results from Dewaele but modified as described by Rudd et al. [20]. The grayscale shading corresponds to a relative frequency histogram of sampled pressure-temperature phase space by the Pb in the simulation. The contours show the temporal evolution through P-T space; ranges are given in the upper-right inset. The portion of the Hugoniot plotted in solid is taken from Dai et al. [21]; the dot-dashed portion is calculated using data from Marsh et al. [22] The bottom-right inset shows the agreement between the velocity observed from a witness sample and corresponding LASNEX simulation.

Figure 3. X-ray radiograph data from N171025-02. Pb (top) and Pb-4wt%Sb (bottom) ripples are boxed in red; Pb and Pb-4wt%Sb step foils in purple; the Au knife edge in gold; and undriven Pb-4wt%Sb ripples in green. The driven Pb-4wt%Sb region of interest is shown in dashed blue; the background-subtracted lineout (blue) and the ρR (orange) from the corresponding simulation are also shown. The bottom images show the knife edge lineout, the MTF, and the Pb-4wt%Sb lookup table. Uncertainty ($\pm$ 1σ, 3σ, see supplementary materials) is shown in dark and light-shaded blue. The substrate thickness (solid) and observed amplitude (dashed) is shown in red and the steps in orange.

Figure 4. Temporal evolution of (a) pressure and (b) flow stress in Pb from the simulation of N171025-02 ($\sim$1 μm initial ripple amplitude). The color denotes the relative frequency of the Pb pressure and flow stress, respectively, at that time as sampled from the simulation. Panel (a) also shows the calculated GF [unitless] and growth rate [1/10 ns], indicated on the right axis. Two pressure history tracer particles, which are initialized 2 μm from a ripple peak (front) and rear surface (back) are also shown in (a). The right axis of (b) indicates the flow stress normalized to the ambient yield stress, Y_0.

Figure 5. Growth factor data for Pb (blue squares) and Pb-4wt%Sb (orange circles) with $\sim$0.4 μm initial ripple amplitude and hydrodynamics simulations using no strength, fcc-based Pb SG model, and the bcc-based Pb ISG model. Discontinuities in the simulation curves are due to shot-to-shot variations. The inset shows full growth factor curves for 65 ns delay with an additional simulation curve using Pb ISG with Pb-4wt%Sb initial density (11.15 g/cm^3). Driven ripple growth data for 55 ns and 65 ns experiments is shown bottom-right.

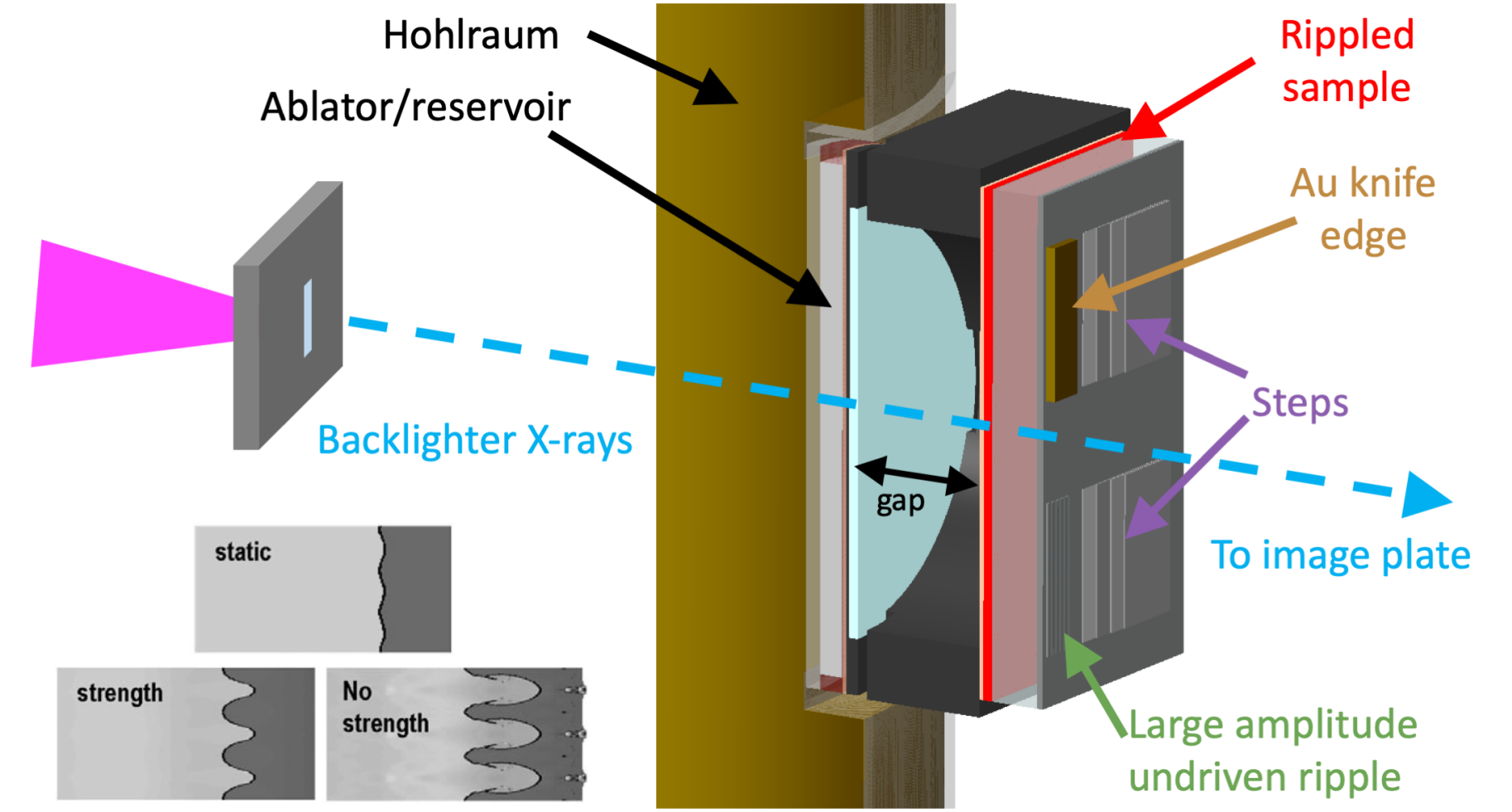
Hohlraum
Ablator/reservoir
Rippled sample
Au knife edge
Backlighter X-rays
gap
Steps
To image plate
static
strength
No strength
Large amplitude undriven ripple

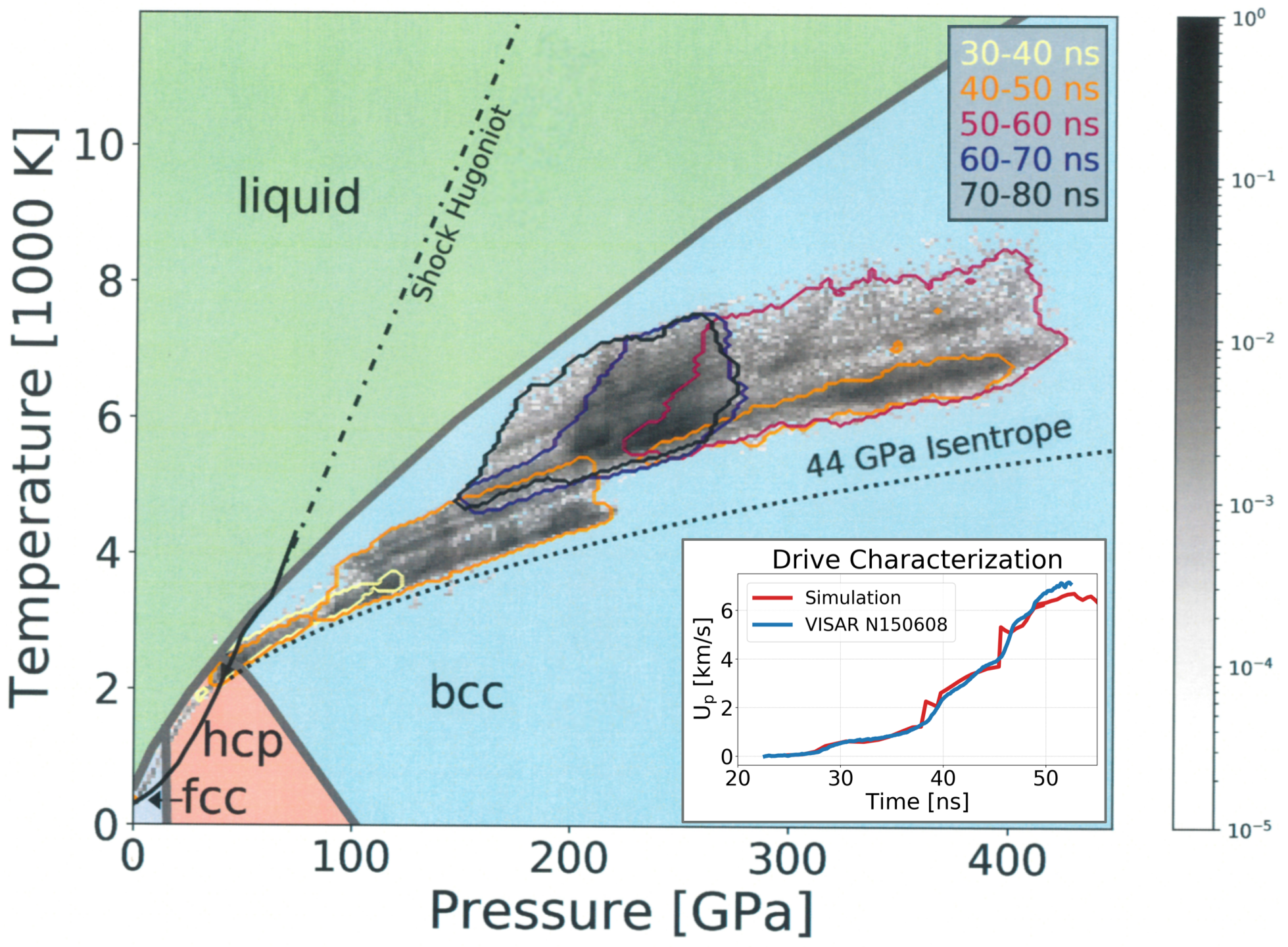
30-40 ns
40-50 ns
50-60 ns
60-70 ns
70-80 ns
liquid
Shock Hugoniot
44 GPa Isentrope
bcc
hcp
fcc
Drive Characterization
Simulation
VISAR N150608
U_p [km/s]
Time [ns]
Temperature [1000 K]
Pressure [GPa]
0
2
4
6
8
10
0
100
200
300
400
20
30
40
50
10^{0}
10^{-1}
10^{-2}
10^{-3}
10^{-4}
10^{-5}

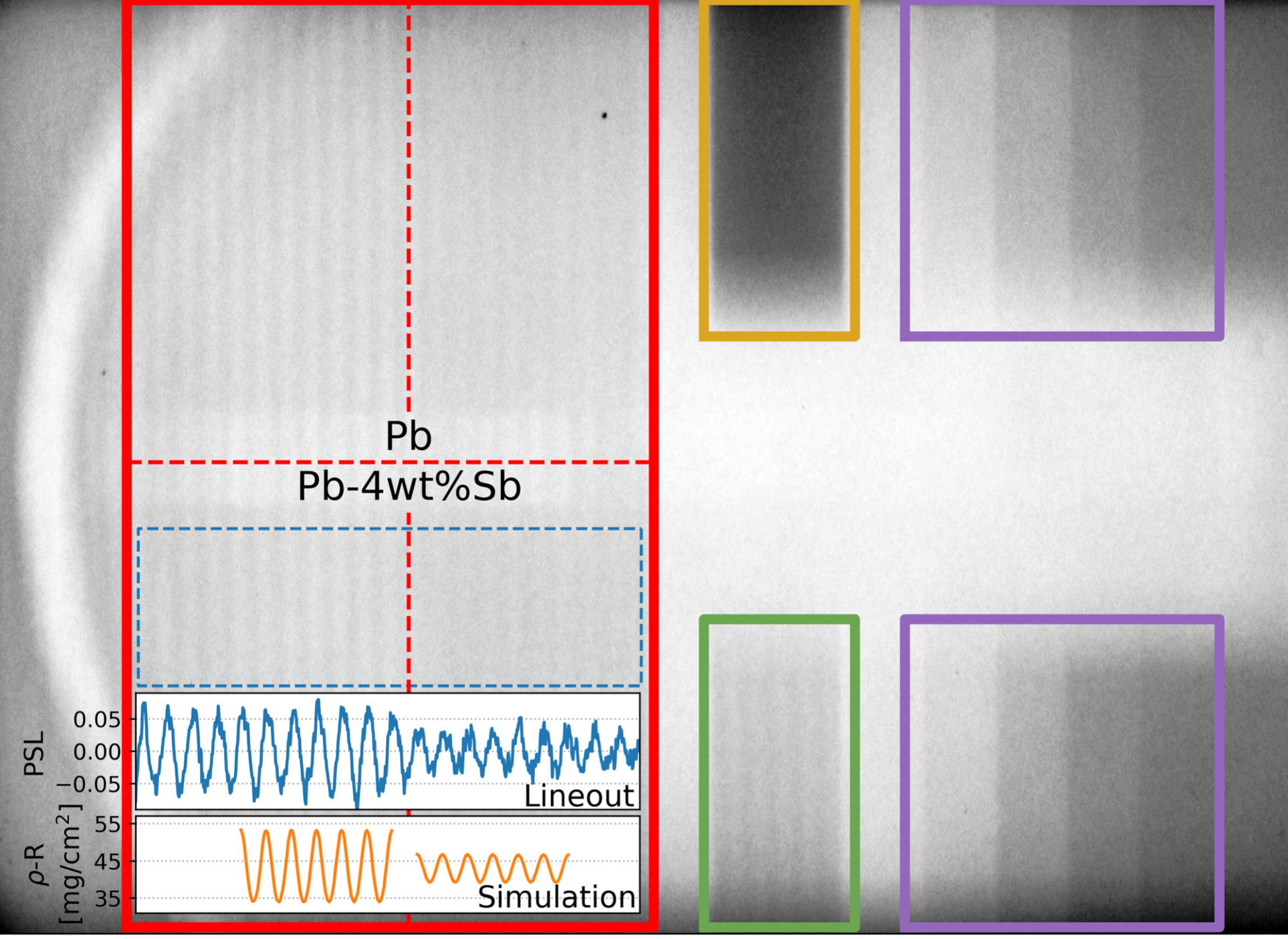
Pb
Pb-4wt%Sb
PSL
0.05
0.00
−0.05
Lineout
ρ-R
[mg/cm²]
55
45
35
Simulation

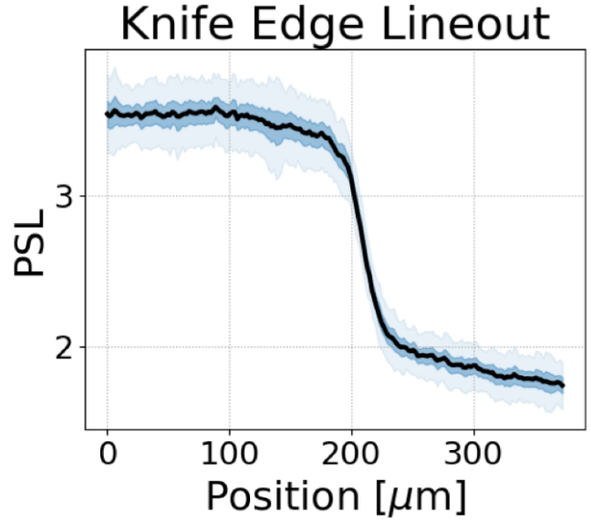
Knife Edge Lineout
PSL
3
2
0
100
200
300
Position [μm]

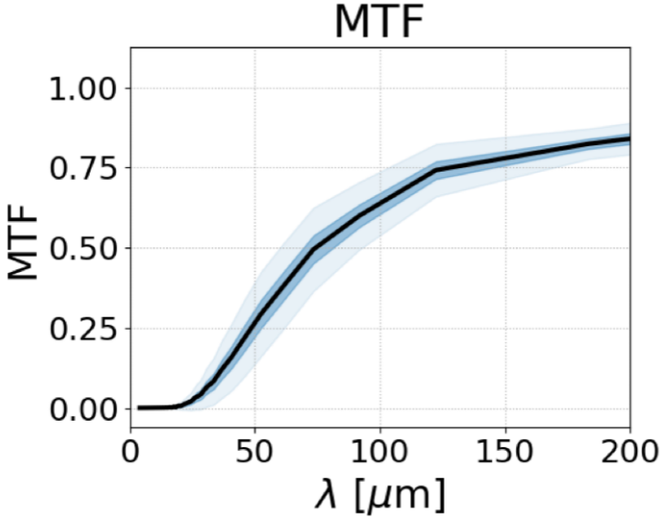
MTF
MTF
1.00
0.75
0.50
0.25
0.00
0
50
100
150
200
λ [μm]

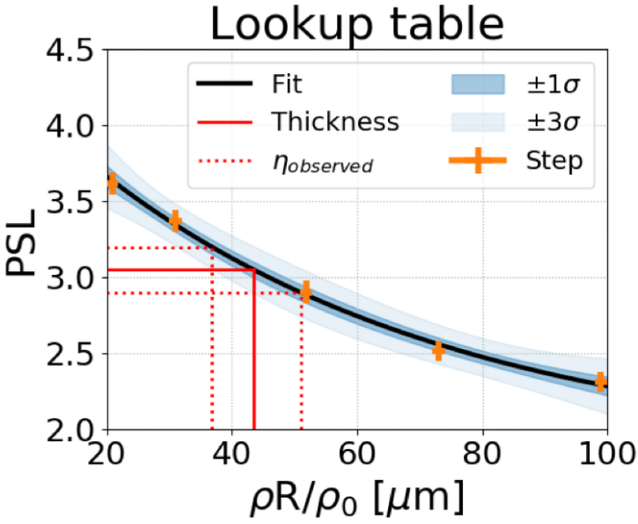
Lookup table
PSL
4.5
4.0
3.5
3.0
2.5
2.0
20
40
60
80
100
ρR/ρ₀ [μm]
Fit
Thickness
η_observed
±1σ
±3σ
Step

Simulated Pb Pressure

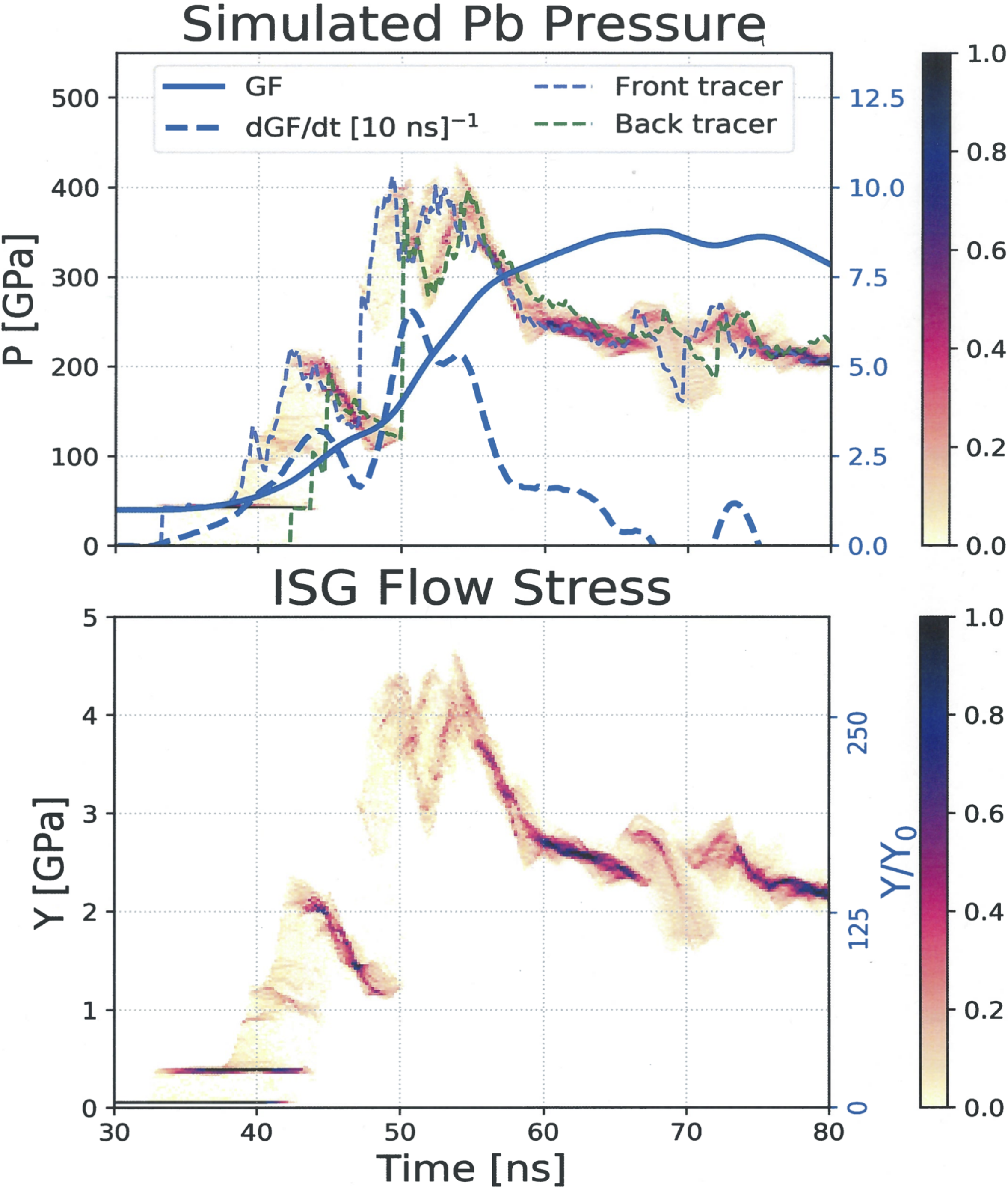

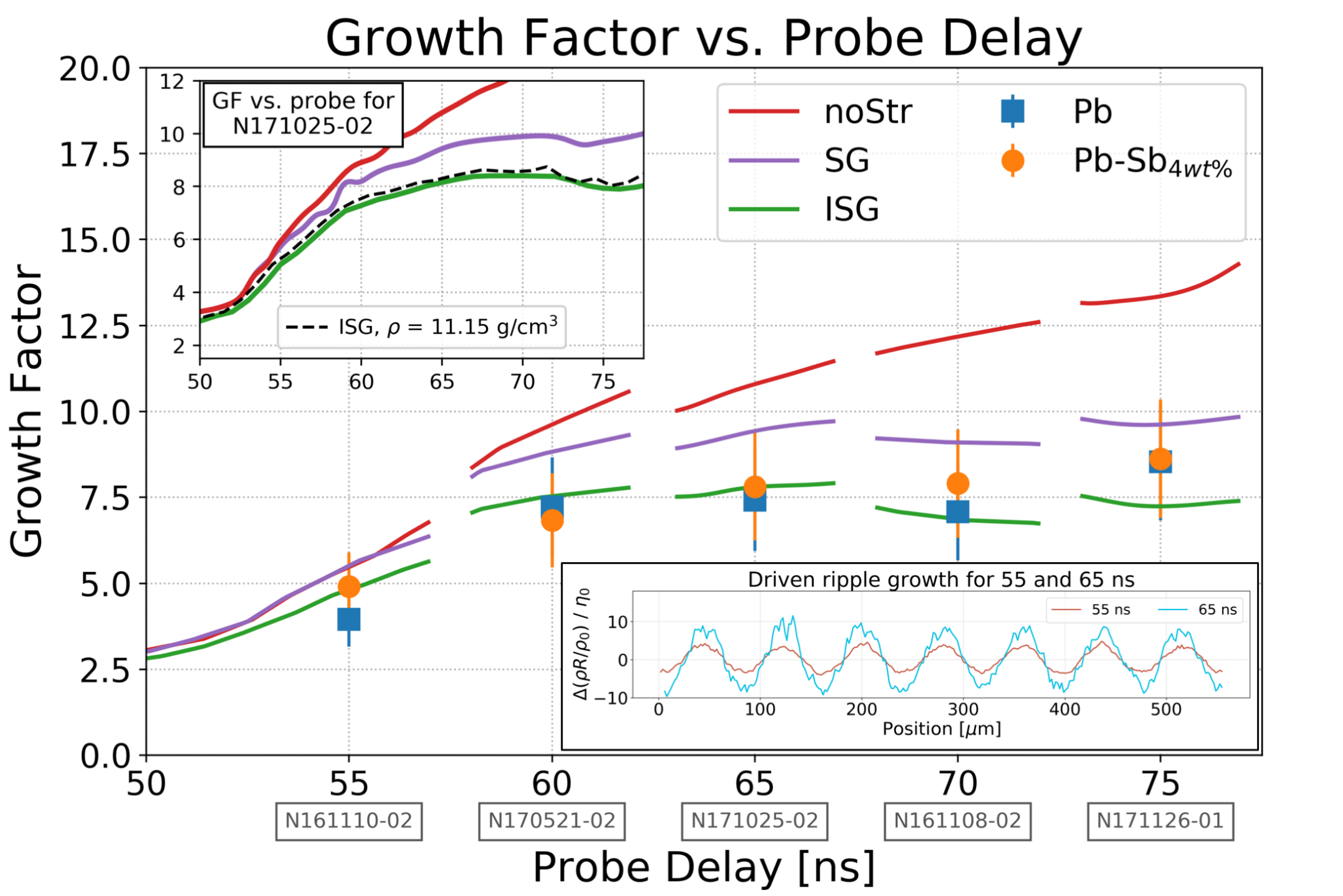
Growth Factor vs. Probe Delay
Growth Factor
Probe Delay [ns]
noStr
SG
ISG
Pb
Pb-Sb4wt%
GF vs. probe for N171025-02
ISG, ρ = 11.15 g/cm3
Driven ripple growth for 55 and 65 ns
Δ(ρR/ρ0) / η0
55 ns
65 ns
Position [μm]
N161110-02
N170521-02
N171025-02
N161108-02
N171126-01